Shock Waves (2018) 28:545–558
DOI 10.1007/s00193-017-0799-4

ORIGINAL ARTICLE

Simulation and scaling analysis of a spherical particle-laden blast wave

Y. Ling[1] · **S. Balachandar**[2]

Received: 14 July 2017 / Revised: 1 December 2017 / Accepted: 22 December 2017 / Published online: 7 February 2018

Abstract A spherical particle-laden blast wave, generated by a sudden release of a sphere of compressed gas–particle mixture, is investigated by numerical simulation. The present problem is a multiphase extension of the classic finite-source spherical blast-wave problem. The gas–particle flow can be fully determined by the initial radius of the spherical mixture and the properties of gas and particles. In many applications, the key dimensionless parameters, such as the initial pressure and density ratios between the compressed gas and the ambient air, can vary over a wide range. Parametric studies are thus performed to investigate the effects of these parameters on the characteristic time and spatial scales of the particle-laden blast wave, such as the maximum radius the contact discontinuity can reach and the time when the particle front crosses the contact discontinuity. A scaling analysis is conducted to establish a scaling relation between the characteristic scales and the controlling parameters. A length scale that incorporates the initial pressure ratio is proposed, which is able to approximately collapse the simulation results for the gas flow for a wide range of initial pressure ratios. This indicates that an approximate similarity solution for a spherical blast wave exists, which is independent of the initial pressure ratio. The approximate scaling is also valid for the particle front if the particles are small and closely follow the surrounding gas.

Keywords Blast wave · Particle-laden flows · Scaling analysis · Eulerian–Lagrangian simulation

1 Introduction

When a compressed gas–particle mixture is suddenly released to a low-pressure atmosphere, a particle-laden blast wave will be generated. Blast phenomena that involve a high-speed particle-laden flow are seen in nature and industrial applications, such as volcanic eruptions [1], dusty explosions [2], and metallic explosive detonations [3,4]. Understanding the physics of a particle-laden blast wave and being able to predict the motions of the gas and the particles are critical to these applications.

In the present study, a blast wave in a simple geometry is considered, i.e., a spherical capsule that contains a gas–particle mixture of high pressure is suddenly released, see Fig. 1. The single-phase analog of the present problem is a classic problem in the literature. The problem of a spherical blast wave generated from a compressed gas sphere was first studied numerically by Brode [5]. The problem has also been referred to as the "spherical shock-tube blast" [6] (due to similarity with the planar shock-tube problem) and also as the "bursting-sphere blast" [7], and was later investigated extensively by many others, including an experimental study by Boyer [8], numerical studies by Brode [9] and Liu et al. [10], and (approximately) analytical investigations by Friedman [11] and McFadden [12].

When the sphere of compressed gas is released, a shock wave (the so-called main shock), an expansion fan, and a contact discontinuity are generated, see Fig. 2. The main shock wave and the contact discontinuity travel outward with decreasing speeds due to the radial expansion effect. Due to the over-expansion arising from the radial effect, a secondary

Communicated by D. Frost and A. Higgins.

✉ Y. Ling
stanley_ling@baylor.edu

[1] Department of Mechanical Engineering, Baylor University, Waco, TX 76798, USA

[2] Department of Mechanical and Aerospace Engineering, University of Florida, Gainesville, FL 32611, USA

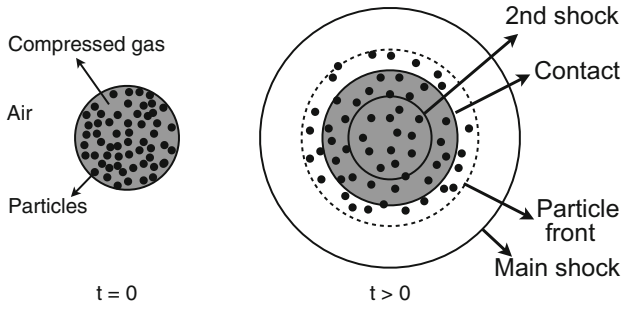

Fig. 1 Schematic of particle dispersal by a spherical blast wave

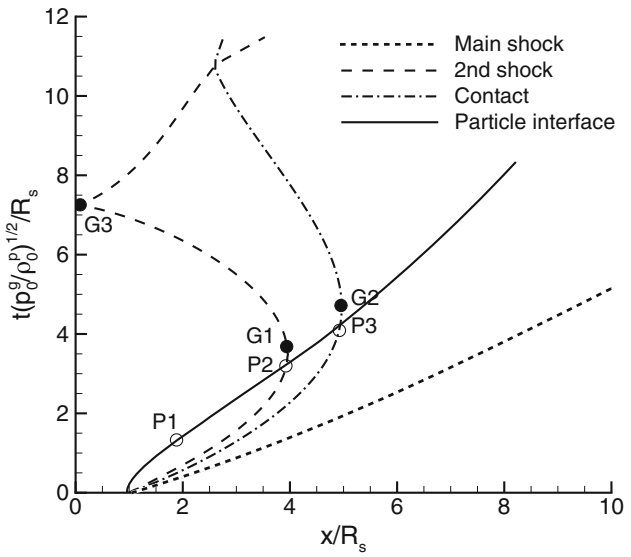

Fig. 2 A representative x–t diagram of spherical particle-laden blast wave. Characteristic time and spatial scales for the gas and particle motion are indicated by filled and unfilled circles. G1: when the secondary shock reaches its maximum radial distance; G2: when the gas contact discontinuity reaches its maximum radial distance; G3: when the secondary shock reaches the origin; P1: when the particle front reaches its maximum velocity; P2: when the particle front crosses the secondary shock; P3: when the particle front crosses the contact discontinuity. Here the initial radius of the spherical mixture, R_s, and $\sqrt{p_0^g/\rho_0^g}$ serve as typical length and velocity scales, respectively

shock wave is formed at the outer boundary of the expansion fan. The secondary shock wave is an imploding shock in nature, yet due to the large initial gas velocity, the secondary shock is initially swept outward before eventually turning inward. The secondary shock wave is reflected at the origin and will move outward again. The reflected secondary shock will interact with the inward-propagating contact discontinuity and pushes the latter outward again. During the interaction, a reflected and a transmitted shock wave are generated. Then a similar cycle starts, with the transmitted shock playing the role of the main shock and the reflected shock playing the role of the secondary shock. This interaction process continues to create a system of reflected and transmitted shocks that become weaker with each interaction. Through these interactions, the gas bounded by the contact discontinuity continues to expand and compress until it asymptotically approaches a stationary state [9].

The present problem can be considered as the multiphase extension of the classic spherical blast-wave problem, where the sphere of compressed gas is now replaced by a mixture of compressed gas and particles. With the addition of particles, the problem becomes more complex [7,13]. Once the compressed gas–particle mixture is released, the particles are driven by the gas flow and are dispersed outward rapidly. In the limit of zero inertia, the particles remain in a mechanical equilibrium with the gas initially inside the sphere, and as a result, the surface separating regions with and without particles (hereafter referred to as "particle front") will overlap with the gas contact discontinuity. However, as long as the particle inertia is finite, then the particle front will first lag behind but later catch up and overtake the contact discontinuity. Furthermore, the particles will also interact with the secondary shock wave since the latter initially move outward but will eventually turn back. These interactions between particles and characteristic waves in a blast make the particle motion complex and hard to predict.

For particle-laden blast waves arising from detonation of multiphase explosives, the gaseous detonation products and particles are substantially accelerated by the detonation wave [14–17]. As a consequence, at the completion of detonation when the blast wave is generated, the initial velocity of gas and particles is not zero within the sphere. Scaling relations for the particle dynamics due to the interaction with the detonation wave have been developed by Tanguay et al. [18]. In the present problem, the gas–particle mixture is considered to be initially quiescent; therefore, the early-term blast dynamics will not be fully represented. Nevertheless, the present problem is expected to capture the long-term dynamics of a particle-laden blast and is also relevant to other blast phenomena such as volcanic eruptions.

In the present study, the spherical particle-laden blast wave is investigated by numerical simulations. Since a large number of particles are involved and the scales of interest are generally much larger than the particle size, the point-particle approach, in which particles are modeled as point masses, is employed here. As flows at the particle scale are not resolved, the interphase momentum and energy coupling must be accurately represented by particle force and heat-transfer models, see [19].

In the present problem, since particles interact with the secondary shock wave, the interphase coupling models used in simulation must be able to rigorously capture shock–particle interaction. (In some particle-laden blast applications, the particles have even been observed to overtake even the main shock wave [3,4].) Significant research progress has been made in particle force modeling in compressible

flows involving shock–particle interaction in recent years. Parmar et al. [20,21] have derived an analytical expression of the particle force in compressible flows at the asymptotic limit of zero Reynolds and Mach numbers. More recently, Annamalai and Balachandar [22] extended the theory to viscous compressible flows and provided a general Faxén form of the particle force. These studies provide a theoretical base to develop physics-based interphase force models at finite Reynolds and Mach numbers. Extensions of the interphase coupling models to finite Reynolds and Mach numbers have been proposed by Parmar et al. [23,24] and Ling et al. [25,26]. The new model is validated against experiments and direct numerical simulation of shock interaction with a single particle [14,27] and with a dense particle curtain [26]. Compared to the conventional models like standard drag [28] and heat-transfer [29] correlations, a significant improvement of the new model is that the unsteady forces and heat-transfer contributions are accounted for in the interphase momentum and energy transfer. Detailed discussions on the importance of different interphase force and heat-transfer contributions are systematically discussed in Ling et al. [30,31]. The unsteady contributions have been shown to be critical to accurate prediction of motion of particles subjected to an incident shock wave [25,26].

The problem of a spherical particle-laden wave has been investigated numerically by Ling et al. [13]. The focus of the previous work is on testing the interphase coupling model and evaluating the importance of unsteady force and heat-transfer contributions on predicting the particle dispersal by a spherical blast wave. As an extension of our previous work [13], the goal of this paper is to conduct a parametric study of the initial conditions and the particle properties and to investigate the effects of these key parameters on particle dispersion in response to the blast wave. The present problem involves multiple parameters that can vary over a wide range, e.g., pressure and temperature of the compressed gas, particle diameter and density, and the initial radius of the spherical mixture. It is difficult to cover each combination of these parameters by simulations even for this simplified setup. A scaling analysis is therefore conducted aiming at reducing the number of independent parameters. Due to the complexity of the present problem, universal scaling or exact similarity solutions do not exist. Nevertheless, it is found that for some region in the parameter space, we are able to collapse solutions for different initial conditions approximately.

A numerical investigation of a similar multiphase bursting-sphere problem has also been reported by Zarei and Frost [32]. The focus of their work was on the effect of secondary energy release from reactive metal particles on the propagation of the blast front. In the present study, we consider only inert particles and are mainly interested in the dispersion of the particles and the scaling behaviors of the compressible multiphase flows generated.

The physical model and numerical methods are to be presented in Sect. 2. The results of the present simulations and the scaling analysis are shown in Sect. 3. We will first address the general scaling results and the approximate ones. Finally, we will conclude the main findings in Sect. 4.

2 Governing equations and numerical methods

2.1 Assumptions

In the present study, the particles are assumed to be spherical, rigid, and inert. The particles are initially uniformly distributed inside the spherical container and are in thermal equilibrium with the compressed gas. The blast wave is considered to occur in an unbounded domain. The gravity effect is neglected. Therefore, the particle-laden flow in the present problem is strictly spherically symmetric at all times.

The gas is assumed to obey the ideal gas law. The gas flow at the macroscale is considered as inviscid, while for the interaction between a particle and the surrounding gas at the microscale (particle scale) viscous effects are included through appropriate models discussed below. For simplicity, the thermal and transport properties of the gas are assumed to be constant.

According to the scaling analysis on interphase momentum and energy coupling [30,31], the mass fraction of particles can serve as a measure of the backward effect of the particles to the gas. In the present study, we focus on the dilute regime where the particle mass fraction is small. Therefore, the gas and particles can be considered to be one-way coupled. We further assume the particle volume fraction to be small, so that particle collisions can be ignored.

It should be mentioned that for many particle-laden blast applications, the initial particle mass fraction is substantial and thus the backward coupling effect cannot be neglected. The particle mass fraction will decrease rapidly when the particles are dispersed outward, and as a consequence, the influence of particles to the gas flows will also drop very fast. For such cases, the one-way coupling approximation adopted here will only be proper for the long-term behavior.

2.2 Governing equations

The governing equations for the one-way coupled compressible particle-laden flows are presented below. The details of the force and heat-transfer models can be found in our previous works [13,14,25,26].

The gas flow is governed by the Euler equations, which can be written as

$$\frac{\partial \rho^{\mathrm{g}}}{\partial t} + \frac{\partial \rho^{\mathrm{g}} u^{\mathrm{g}}}{\partial x} + 2\frac{\rho^{\mathrm{g}} u^{\mathrm{g}}}{x} = 0, \tag{1}$$

$$\frac{\partial \rho^{\mathrm{g}} u^{\mathrm{g}}}{\partial t} + \frac{\partial \rho^{\mathrm{g}} (u^{\mathrm{g}})^2}{\partial x} + 2\frac{\rho^{\mathrm{g}} (u^{\mathrm{g}})^2}{x} = -\frac{\partial p^{\mathrm{g}}}{\partial x}, \tag{2}$$

$$\frac{\partial \rho^{\mathrm{g}} E^{\mathrm{g}}}{\partial t} + \frac{\partial \rho^{\mathrm{g}} H^{\mathrm{g}} u^{\mathrm{g}}}{\partial x} + 2\frac{\rho^{\mathrm{g}} H^{\mathrm{g}} u^{\mathrm{g}}}{x} 0, \tag{3}$$

where ρ^{g}, u^{g}, p^{g}, E^{g}, and H^{g} represent the density, velocity, pressure, total energy, and total enthalpy of gas, respectively. Throughout the paper, the superscripts "g" and "p" indicate quantities associated with the gas and the particles, respectively.

The Lagrangian point-particle approach is employed to simulate the particulate phase [19,25,33,34]. Different from fully resolved simulations [14,35–37], the particles are modeled as point masses and the corresponding position, momentum, and energy equations of which are given as

$$\frac{\mathrm{d}x^{\mathrm{p}}}{\mathrm{d}t} = u^{\mathrm{p}}, \tag{4}$$

$$\frac{\mathrm{d}u^{\mathrm{p}}}{\mathrm{d}t} = f = f_{\mathrm{qs}} + f_{\mathrm{pg}} + f_{\mathrm{am}} + f_{\mathrm{vu}}, \tag{5}$$

$$\frac{\mathrm{d}T^{\mathrm{p}}}{\mathrm{d}t} = q = q_{\mathrm{qs}} + q_{\mathrm{uu}} + q_{\mathrm{du}}, \tag{6}$$

where x^{p}, u^{p}, and T^{p} represent position, velocity, and temperature of an individual particle, respectively. The force per unit mass and heat transfer per unit heat capacity are denoted by f^{p} and q^{p}, respectively. In the above expressions, f_{qs}, f_{pg}, f_{am}, and f_{vu} represent the quasi-steady, pressure gradient, added-mass, and viscous-unsteady contributions to the force, respectively. Similarly, the quasi-steady, undisturbed-unsteady, and diffusive-unsteady contributions to the overall heat transfer are denoted by q_{qs}, q_{uu}, and q_{du}.

The expressions for the force contributions are

$$f_{\mathrm{qs}} = \frac{\overline{u^{\mathrm{g}}}^{\mathrm{s}} - u^{\mathrm{p}}}{\tau^{\mathrm{p}}} \frac{C_{\mathrm{D}} \mathrm{Re}^{\mathrm{p}}}{24}, \tag{7}$$

$$f_{\mathrm{pg}} = -\frac{1}{\rho^{\mathrm{p}}} \frac{\overline{\mathrm{D}(\rho^{\mathrm{g}} u^{\mathrm{g}})}^{\mathrm{v}}}{\mathrm{D}t}, \tag{8}$$

$$f_{\mathrm{am}} = \frac{C_M}{\rho^{\mathrm{p}}} \left(-\frac{\overline{D(\rho^{\mathrm{g}} u^{\mathrm{g}})}^{\mathrm{v}}}{Dt} - \frac{\mathrm{d}}{\mathrm{d}t} \overline{(\rho^{\mathrm{g}} u^{\mathrm{p}})}^{\mathrm{v}} \right), \tag{9}$$

$$f_{\mathrm{vu}} = \sqrt{\frac{\rho^{\mathrm{g}}}{\rho^{\mathrm{p}}}} \sqrt{\frac{\tau_{\mathrm{vu}}}{\tau^{\mathrm{p}}}} \frac{3}{\sqrt{2\pi}\rho^{\mathrm{g}}} \int_{-\infty}^{t} K_{\mathrm{vu}} \left(\frac{t-\xi}{\tau_{\mathrm{vu}}}, \mathrm{Re}^{\mathrm{p}} \right) \left(-\frac{\overline{\mathrm{D}(\rho^{\mathrm{g}} u^{\mathrm{g}})}^{\mathrm{s}}}{\mathrm{D}t} - \frac{\mathrm{d}}{\mathrm{d}t} \overline{(\rho^{\mathrm{g}} u^{\mathrm{p}})}^{\mathrm{s}} \right) \frac{\mathrm{d}\xi}{\tau_{\mathrm{vu}}}, \tag{10}$$

where the quasi-steady drag coefficient C_{D} is a function of the particle Reynolds number Re^{p} and Mach number M^{p} [24]. The definitions of Re^{p} and M^{p} are given as

$$\mathrm{Re}^{\mathrm{p}} = \frac{\rho^{\mathrm{g}} |u^{\mathrm{p}} - \overline{u^{\mathrm{g}}}^{\mathrm{s}}| d^{\mathrm{p}}}{\mu^{\mathrm{g}}}, \tag{11}$$

and

$$M^{\mathrm{p}} = \frac{|u^{\mathrm{p}} - \overline{u^{\mathrm{g}}}^{\mathrm{s}}|}{a^{\mathrm{g}}}. \tag{12}$$

For one-way coupled simulations, $\mathrm{D}(\rho^{\mathrm{g}} u^{\mathrm{g}})/\mathrm{D}t$ is approximated by $\partial p^{\mathrm{g}}/\partial x$. Bars with a superscript "s" or "v" denote gas quantities averaged over the particle surface S^{p} or volume V^{p} [22], respectively, i.e.,

$$\overline{u^{\mathrm{g}}}^{\mathrm{s}} = \frac{1}{S^{\mathrm{p}}} \oint_{S^{\mathrm{p}}} u^{\mathrm{g}} \mathrm{d}S, \tag{13}$$

$$\overline{u^{\mathrm{g}}}^{\mathrm{v}} = \frac{1}{V^{\mathrm{p}}} \int_{V^{\mathrm{p}}} u^{\mathrm{g}} \mathrm{d}V. \tag{14}$$

In (7) and (10), τ^{p} is the particle response time, expressed as

$$\tau^{\mathrm{p}} = \frac{\rho^{\mathrm{p}} (d^{\mathrm{p}})^2}{18\mu^{\mathrm{g}}}. \tag{15}$$

The effective added-mass coefficient C_{M} is a function of M^{p} as [14]

$$C_M = C_{M,0} \left(1 + 1.8(M^{\mathrm{p}})^2 + 7.6(M^{\mathrm{p}})^4 \right), \tag{16}$$

where $C_{M,0} = 1/2$ is the added-mass coefficient for a spherical particle at $M^{\mathrm{p}} = 0$.

The viscous-unsteady force kernel is denoted by K_{vu}, and here the finite-Reynolds-number model of K_{vu} suggested by Mei and Adrian [38] is employed,

$$K_{\mathrm{vu}}(t/\tau_{\mathrm{vu}}) = \frac{1}{[(t/\tau_{\mathrm{vu}})^{1/4} + t/\tau_{\mathrm{vu}}]^2}. \tag{17}$$

where τ_{vu} is the particle viscous-unsteady time scale, defined as [31]

$$\tau_{\mathrm{vu}} = \frac{(d^{\mathrm{p}})^2}{\nu^{\mathrm{g}}} \left(\frac{4}{\pi} \right)^{1/3} \left(\frac{0.75 + 0.105\mathrm{Re}^{\mathrm{p}}}{\mathrm{Re}^{\mathrm{p}}} \right)^2. \tag{18}$$

The expressions of the heat-transfer contributions are

$$q_{\mathrm{qs}} = \frac{\overline{T^{\mathrm{g}}}^{\mathrm{s}} - T^{\mathrm{p}}}{\tau_\theta^{\mathrm{p}}} \frac{\mathrm{Nu}}{2}, \tag{19}$$

$$q_{\mathrm{uu}} = \frac{1}{\rho^{\mathrm{p}} C^{\mathrm{p}}} \frac{\overline{\partial q^{\mathrm{g}}}^{\mathrm{v}}}{\partial x}, \tag{20}$$

$$q_{\mathrm{du}} = \frac{\tau_{\mathrm{du}}}{\tau_\theta^{\mathrm{p}}} \frac{\mathrm{Pe}^{\mathrm{p}}}{2\rho^{\mathrm{g}}} \int_{-\infty}^{t} K_{\mathrm{du}} \left(\frac{t-\xi}{\tau_{\mathrm{du}}}, \mathrm{Pe}^{\mathrm{p}} \right) \left(\frac{1}{C^{\mathrm{g}}} \frac{\overline{\partial q^{\mathrm{g}}}^{\mathrm{s}}}{\partial x} - \frac{\mathrm{d}}{\mathrm{d}t} \overline{(\rho^{\mathrm{g}} T^{\mathrm{p}})}^{\mathrm{s}} \right) \frac{\mathrm{d}\xi}{\tau_{\mathrm{du}}}, \tag{21}$$

where Nu is the Nusselt number. The empirical correlation of Fox et al. [39] is used to calculate Nu at finite Re^{p} and M^{p}. In (19) and (21), τ_θ^{p} is the particle thermal response time,

$$\tau_\theta^{\mathrm{p}} = \frac{\rho^{\mathrm{p}} C^{\mathrm{p}} (d^{\mathrm{p}})^2}{12 k^{\mathrm{g}}}. \tag{22}$$

Since here the gas flow at macroscale is considered as inviscid, $\partial q^{\mathrm{g}}/\partial x = 0$. As a result, $q_{\mathrm{uu}} = 0$. The diffusive-unsteady thermal kernel is denoted by K_{du}, and the model of Feng and Michaelides [40] is employed,

$$K_{\mathrm{du}}(t/\tau_{\mathrm{du}}) = \frac{\exp(-t/\tau_{\mathrm{du}})}{\sqrt{\pi (t/\tau_{\mathrm{du}})}} - \mathrm{erfc}(\sqrt{t/\tau_{\mathrm{du}}}), \tag{23}$$

where τ_{du} is the diffusive-unsteady timescale, defined as

$$\tau_{\mathrm{du}} = \frac{(d^{\mathrm{p}})^2}{\alpha^{\mathrm{g}}} \frac{4}{(\mathrm{Pe}^{\mathrm{p}})^2}. \tag{24}$$

It is noted that the interphase heat-transfer model [(19)–(24)] is shown here just for completeness, but the thermal behavior of the particles in a blast wave will not be discussed in this work. The present study is focused on the mechanical response of particles in a spherical blast wave.

2.3 Numerical methods

The numerical approach for the Euler equation is based on the cell-centered finite-volume methodology. The inviscid flux for the gas is calculated by the approximate Riemann solver of Roe [41]. The face-states are obtained by a simplified second-order accurate weighted essentially non-oscillatory scheme, see, e.g., Jiang and Shu [42], which modifies the gradients computed using the least-squares reconstruction method of Barth [43]. The time-integration method for the gas and particle equations is the fourth-order Runge–Kutta method. The solution method has been extensively verified and validated for gas and gas–particle flows with and without shock waves. For brevity, the results from these studies are not reproduced here. For more details, see Haselbacher [44], Haselbacher et al. [45], and Ling et al. [46].

2.4 Simulation setup

The computational domain is one dimensional in the radial direction. The spherical symmetric boundary condition is invoked at $x = 0$. Thanks to the low computational cost of one-dimensional simulations, the outer boundary is made sufficiently large, so that the main shock wave never reaches the outer boundary. The cell size is taken to be 0.1 mm, which has been verified for yielding grid-independent results. The time step is calculated based on the CFL condition, with the CFL number equal to 0.3.

3 Simulation results and scaling analysis

3.1 Characteristic time and spatial scales

Before showing the simulation results, we first introduce the characteristic time and spatial scales of interest for a spherical particle-laden blast wave. Figure 2 shows a representative particle-laden flow field in a x–t diagram. The trajectories of the main shock wave, the contact discontinuity, and the secondary shock wave are shown along with the trajectory of the particle front. Different from the main shock wave that continues to propagate outward, the contact discontinuity and the secondary shock wave first move outward and then turn back toward the origin. As a consequence, three points in the x–t diagram are chosen to characterize the gas flow:

- G1: the time and radial location for the secondary shock reaching the maximum distance
- G2: the time and radial location for the contact discontinuity reaching the maximum distance
- G3: the time for the secondary shock reaching the origin.

As described above in Sect. 1, after the reflected secondary shock wave interacts with the contact discontinuity, subsequent wave interaction cycles follow. Though the later wave interactions are also interesting, here we focus on the early behavior before the reflected secondary shock wave interacts with the contact discontinuity.

Another three characteristic points are picked in the x–t diagram to characterize the dynamics of the particle front:

- P1: the time and radial location when the particle front reaches its maximum velocity
- P2: the time and radial location when the particle front crosses the secondary shock
- P3: the time and radial location when the particle front crosses the contact discontinuity.

The volume fraction, velocity, and temperature profiles of particles within the particle front have been studied extensively in the previous work [13]; here, we mainly focus on the motion of the particle front. The reasons for choosing these three points to characterize the particle front motion are given as follows. The particle front typically accelerates very fast initially and then slows down gradually, so P1 represents the peak velocity that the particle front can reach. Though the instability of the contact discontinuity is out of the scope of this study, the decelerating contact discontinuity is indeed unstable due to the Rayleigh–Taylor instability (RTI) [47]. When the particle front overtakes the contact discontinuity, the particles further perturb the unstable contact

discontinuity and influence the development of RTI. Therefore, the intersection point between the particle front and the contact discontinuity (P2) is important to many blast applications. Similarly, the secondary shock wave is a spherical imploding shock, which is also unstable, see [48]. Therefore, the intersection between the particle front and the secondary shock (P3) is also of great interest in terms of stability of the converging secondary shock. Furthermore, it has been reported that the particle front in a blast is also unstable, see [49,50]. Therefore, the interactions of the particle front with the contact discontinuity and the secondary shock wave may also in turn influence the instability development at the particle front.

In the present study, the particles will not influence the instability due to the one-way coupling approximation. Nevertheless, being able to predict the interaction time and the flow properties when the particle front interacts with the secondary shock or the contact discontinuity is critical to estimating the growth rate of perturbation. Application of the present results to stability analysis is deferred to our future work.

3.2 Scaling for the gas flow

Due to the one-way coupling assumption, the gas phase is independent of the particle phase, and thus, a gas-related quantity q can be expressed as a function of independent gas properties that define the problem as

$$q^{\mathrm{g}} = q^{\mathrm{g}}\left(p_4^{\mathrm{g}}, \rho_4^{\mathrm{g}}, \gamma_4, p_0^{\mathrm{g}}, \rho_0^{\mathrm{g}}, \gamma_0, R_{\mathrm{s}}, x, t\right), \tag{25}$$

where p_4^{g}, ρ_4^{g}, γ_4, and p_0^{g}, ρ_0^{g}, γ_0 denote the initial pressure and density, and specific heat ratio of the compressed gas and ambient air, see Fig. 1. The initial radius of the spherical gas–particle mixture is denoted by R_{s}.

If p_0^{g}, ρ_0^{g}, and R_{s} are chosen as to be repeating variables, then (25) can be written into dimensionless form by applying the Buckingham Π theorem:

$$Q^{\mathrm{g}} = Q^{\mathrm{g}}\left(\frac{p_4^{\mathrm{g}}}{p_0^{\mathrm{g}}}, \frac{\rho_4^{\mathrm{g}}}{\rho_0^{\mathrm{g}}}, \gamma_4, \gamma_0, \frac{x}{R_{\mathrm{s}}}, \frac{t\sqrt{p_0^{\mathrm{g}}/\rho_0^{\mathrm{g}}}}{R_{\mathrm{s}}}\right), \tag{26}$$

where Q^{g} is the dimensionless form of q^{g}. Note that R_{s} and $\sqrt{p_0^{\mathrm{g}}/\rho_0^{\mathrm{g}}}$ serve as typical length and velocity scales, respectively. For example, if we considered the location of the gas contact discontinuity, denoted by x_{gc}, as the dependent variable, then x_{gc} can be expressed as

$$\frac{x_{\mathrm{gc}}}{R_{\mathrm{s}}} = \xi\left(\frac{p_4^{\mathrm{g}}}{p_0^{\mathrm{g}}}, \frac{\rho_4^{\mathrm{g}}}{\rho_0^{\mathrm{g}}}, \gamma_4, \gamma_0, \frac{t\sqrt{p_0^{\mathrm{g}}/\rho_0^{\mathrm{g}}}}{R_{\mathrm{s}}}\right). \tag{27}$$

It should be noted that since R_{s} is the only length scale, for a given initial condition ($p_4^{\mathrm{g}}/p_0^{\mathrm{g}}$ and $\rho_4^{\mathrm{g}}\rho_0^{\mathrm{g}}$) and material properties (γ_4 and γ_0), the trajectories of the gas contact discontinuity, the main shock wave, and the secondary shock all scale linearly with R_{s}.

3.3 Scaling of the particle motion

When particles are added, the particle parameters need to be included to define the dependence of a particle-related quantity q^{p}:

$$q^{\mathrm{p}} = q^{\mathrm{p}}\left(p_4^{\mathrm{g}}, \rho_4^{\mathrm{g}}, \gamma_4, p_0^{\mathrm{g}}, \rho_0^{\mathrm{g}}, \gamma_0, R_{\mathrm{s}}, d^{\mathrm{p}}, \rho^{\mathrm{p}}, x_0^{\mathrm{p}}, \mu^{\mathrm{g}}, x, t\right), \tag{28}$$

where x_0^{p} is the initial location of a particle. The motion of the particles can be fully determined by d^{p}, ρ^{p}, and x_0^{p}. For the gas flow at macroscale, μ^{g} is irrelevant and does not appear in (25). However, viscous effects have to be considered in computing the drag force on a particle.

Similarly, (28) can be written in dimensionless form by applying the Π theorem:

$$Q^{\mathrm{p}} = Q^{\mathrm{p}}\left(\frac{p_4^{\mathrm{g}}}{p_0^{\mathrm{g}}}, \frac{\rho_4^{\mathrm{g}}}{\rho_0^{\mathrm{g}}}, \gamma_4, \gamma_0, \frac{d^{\mathrm{p}}}{R_{\mathrm{s}}}, \frac{\rho^{\mathrm{p}}}{\rho_0^{\mathrm{g}}}, \frac{x_0^{\mathrm{p}}}{R_{\mathrm{s}}}, \mathrm{Re}_{\mathrm{s}}, \frac{x}{R_{\mathrm{s}}}, \frac{t\sqrt{p_0^{\mathrm{g}}/\rho_0^{\mathrm{g}}}}{R_{\mathrm{s}}}\right), \tag{29}$$

where Re_{s} is the Reynolds number based on the initial radius of the gas–particle mixture sphere, which is defined as

$$\mathrm{Re}_{\mathrm{s}} = \frac{\rho_0^{\mathrm{g}}\sqrt{p_0^{\mathrm{g}}/\rho_0^{\mathrm{g}}}R_{\mathrm{s}}}{\mu^{\mathrm{g}}}. \tag{30}$$

For the particle initially located at the edge of the spherical mixture, namely $x_0^{\mathrm{p}} = R_{\mathrm{s}}$, then the trajectory of that particle represents that of the particle front. The location of the particle front at any later time, x_{pf}, thus can be expressed as

$$\frac{x_{\mathrm{pf}}}{R_{\mathrm{s}}} = \eta\left(\frac{p_4^{\mathrm{g}}}{p_0^{\mathrm{g}}}, \frac{\rho_4^{\mathrm{g}}}{\rho_0^{\mathrm{g}}}, \gamma_4, \gamma_0, \frac{d^{\mathrm{p}}}{R_{\mathrm{s}}}, \frac{\rho^{\mathrm{p}}}{\rho_0^{\mathrm{g}}}, \mathrm{Re}_{\mathrm{s}}, \frac{t\sqrt{p_0^{\mathrm{g}}/\rho_0^{\mathrm{g}}}}{R_{\mathrm{s}}}\right), \tag{31}$$

where x_{pf} is a function of Re_{s}, which in turn depends on R_{s}. As a consequence, the particle front location does not scale linearly with R_{s} as the gas contact [see (27)].

3.4 Scaling of the particle front in asymptotic limits

There exist limiting cases where we can simplify the scaling of the particle front.

Inviscid limit It has been shown in [13,31] that inviscid-unsteady forces are dominant at early time after the blast is induced and the early-time acceleration of particles are mainly due to inviscid mechanisms. If only the inviscid forces f_{pg} and f_{am} are active in the particle equation of motion (5), then $\mathrm{Re_s}$ can be eliminated from (29), and we obtain

$$\frac{x_{\mathrm{pf}}}{R_{\mathrm{s}}} = \eta_{\mathrm{inv}}\left(\frac{p_4^{\mathrm{g}}}{p_0^{\mathrm{g}}}, \frac{\rho_4^{\mathrm{g}}}{\rho_0^{\mathrm{g}}}, \gamma_4, \gamma_0, \frac{\rho^{\mathrm{p}}}{\rho_0^{\mathrm{g}}}, \frac{t\sqrt{p_0^{\mathrm{g}}/\rho_0^{\mathrm{g}}}}{R_{\mathrm{s}}}\right). \tag{32}$$

For given initial conditions of the gas and material properties, the particle front location in the inviscid limit turns to scale with R_{s} again.

Stokes limit When the particle diameter is very small ($d^{\mathrm{p}} \to 0$), it is shown in [13,31] that the overall influence of the unsteady forces on particle motion becomes small. Since $\mathrm{Re^p}$ is also small, the particle force reduces to the Stokes drag. In this limit, the viscous effect on the gas–particle interaction can be represented by the particle response time τ^{p}. As a result, (29) can be simplified as

$$\frac{x_{\mathrm{pf}}}{R_{\mathrm{s}}} = \eta_{\mathrm{St}}\left(\frac{p_4^{\mathrm{g}}}{p_0^{\mathrm{g}}}, \frac{\rho_4^{\mathrm{g}}}{\rho_0^{\mathrm{g}}}, \gamma_4, \gamma_0, \mathrm{St^p}, \frac{t\sqrt{p_0^{\mathrm{g}}/\rho_0^{\mathrm{g}}}}{R_{\mathrm{s}}}\right), \tag{33}$$

where $\mathrm{St^p}$ is the particle Stokes number, defined as

$$\mathrm{St^p} = \frac{\tau^{\mathrm{p}}\sqrt{p_0^{\mathrm{g}}/\rho_0^{\mathrm{g}}}}{R_{\mathrm{s}}} = \frac{\rho^{\mathrm{p}}}{18\mu^{\mathrm{g}}}\sqrt{\frac{p_0^{\mathrm{g}}}{\rho_0^{\mathrm{g}}}}\frac{(d^{\mathrm{p}})^2}{R_{\mathrm{s}}}. \tag{34}$$

It is noted that in the Stokes limit, x_{pf} will scale linearly with R_{s} if $\mathrm{St^p}$ is a constant. For given gas property and particle density, it can be seen that $\mathrm{St^p} \sim (d^{\mathrm{p}})^2/R_{\mathrm{s}}$.

Inertial limit For a spherical particle, there exists an inertial regime $750 < \mathrm{Re^p} < 3.5 \times 10^5$ in which the quasi-steady drag coefficient C_{D} is almost constant ($C_{\mathrm{D}} \approx 0.42$), which is referred to as Newton's drag law (see [51]). In this regime, the particle diameter is finite, so the contributions of all forces in (5) need to be taken into account. In this inertial limit, (29 can be simplified as

$$\frac{x_{\mathrm{pf}}}{R_{\mathrm{s}}} = \eta_{\mathrm{iner}}\left(\frac{p_4^{\mathrm{g}}}{p_0^{\mathrm{g}}}, \frac{\rho_4^{\mathrm{g}}}{\rho_0^{\mathrm{g}}}, \gamma_4, \gamma_0, \frac{\rho^{\mathrm{p}}}{\rho_0^{\mathrm{g}}}, \frac{\mathrm{St^p}}{\mathrm{Re^p}}, \frac{t\sqrt{p_0^{\mathrm{g}}/\rho_0^{\mathrm{g}}}}{R_{\mathrm{s}}}\right). \tag{35}$$

Table 1 Simulation cases to examine the scaling of x_{pf} related to of R_{s}

Case	R_{s} (mm)	ρ^{p} (kg/m^3)	d^{p} (μm)
1-1	25.4	1410	1
1-2	25.4	1410	100
1-3	25.4	141	1000
1-4	254	1410	3.162
1-5	254	1410	1000
1-6	254	14,100	1

For all cases here $p_4^{\mathrm{g}}/p_0^{\mathrm{g}} = 121$, $\rho_4^{\mathrm{g}}/\rho_0^{\mathrm{g}} = 121$, and $\gamma_4 = \gamma_0 = 1.4$

It can be observed that the ratio $\mathrm{St^p/Re^p}$ replaces $\mathrm{St^p}$ in (33) to take the finite Reynolds number effect into account, which can be also written in terms of dimensionless variables as:

$$\frac{\mathrm{St^p}}{\mathrm{Re^p}} = \frac{\rho^{\mathrm{p}}/\rho_0^{\mathrm{g}}}{\rho^{\mathrm{g}}/\rho_0^{\mathrm{g}}}\left(\frac{u^{\mathrm{g}} - u^{\mathrm{p}}}{\sqrt{p_0^{\mathrm{g}}/\rho_0^{\mathrm{g}}}}\right)^{-1}\frac{d^{\mathrm{p}}}{R_{\mathrm{s}}}. \tag{36}$$

In this inertial limit, x_{pf} will scale linearly with R_{s} when $d^{\mathrm{p}}/R_{\mathrm{s}}$ is a constant.

3.4.1 Simulation results for the particle front

Numerical simulations are performed to examine the scaling analysis given above. Here, we only focus on the particle front. A summary of cases is given in Table 1. For cases 1-1 to 1-3, $R_{\mathrm{s}} = 25.4$ mm, and for cases 1-4 to 1-6, $R_{\mathrm{s}} = 254$ mm.

Relation between d^{p} and R_{s}. The particle density in cases 1-1, 1-2, 1-4, and 1-5 is the same. The particle diameter for cases 1-1 and 1-4 is chosen to be small, so that they lie in the Stokes limit. According to the scaling analysis above, we have chosen $(d^{\mathrm{p}})^2/R_{\mathrm{s}}$ to be the same as 3.94×10^{-11} for cases 1-1 and 1-4. The evolutions of particle front position and velocity for cases 1-1 and 1-4 are shown in Fig. 3, and it can be seen that temporal evolutions of the particle front location and velocity both collapse very well for these two cases when plotted in dimensionless variables x/R_{s} and $t\sqrt{p_0^{\mathrm{g}}/\rho_0^{\mathrm{g}}}/R_{\mathrm{s}}$, verifying the above scaling argument in the Stokes limit, i.e., (33). The particle fronts for the two cases reach the maximum velocities, $u_{\mathrm{P1}} = 2.15\sqrt{p_0^{\mathrm{g}}/\rho_0^{\mathrm{g}}}$, at $t_{\mathrm{P1}} = 0.55R_{\mathrm{s}}/\sqrt{p_0^{\mathrm{g}}/\rho_0^{\mathrm{g}}}$, when they cross the secondary shock (so P1 overlaps with P2).

On the other hand, the particle diameter for cases 1-2 and 1-5 is fairly large, and the corresponding particle Reynolds numbers at early time are both in the inertial regime. Then according to the scaling analysis, we set $d^{\mathrm{p}}/R_{\mathrm{s}}$ to be the same equal to 3.94×10^{-3} for these two cases. The evolutions of particle front position and velocity for cases 1-2 and 1-5 are shown in Fig. 3a, b, respectively. Again, it is observed that

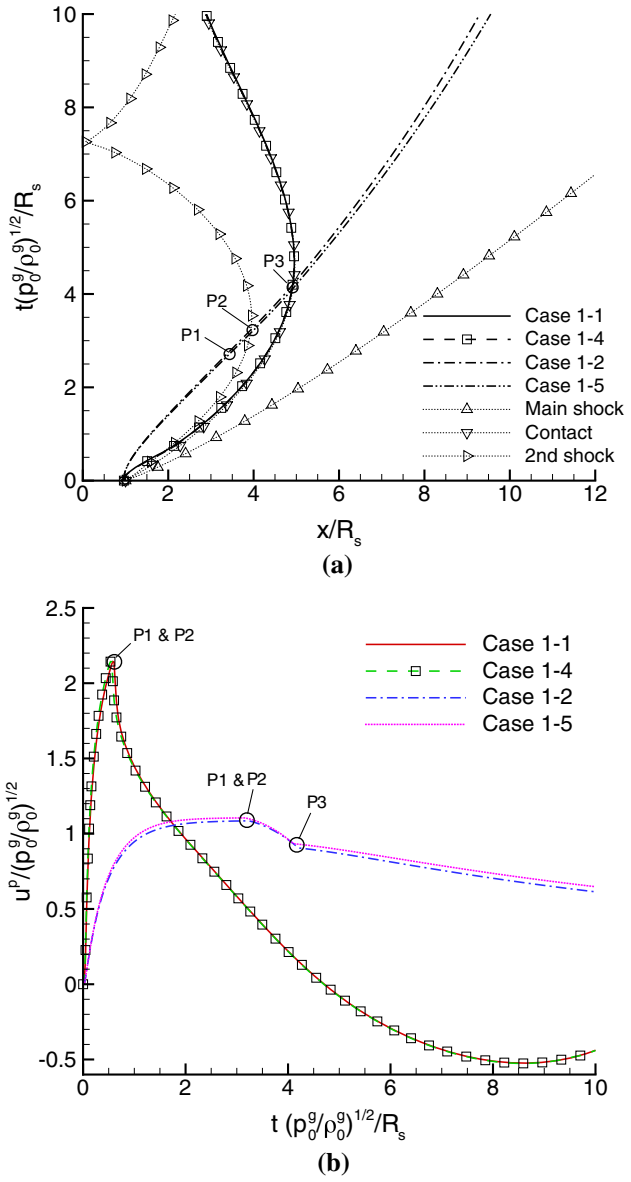

Fig. 3 Evolutions of particle position and velocity for different R_s and d^p with ρ^p fixed at 1410 kg/m^3 for cases 1-1, 1-2, 1-4, and 1-5. Note that $(d^p)^2/R_s$ is identical for cases 1-1 and 1-4, and d^p/R_s is identical for cases 1-2 and 1-5. **a** x–t diagram. **b** u^p evolution

the results collapse very well when plotted in dimensionless variables x/R_s and $t\sqrt{p_0^g/\rho_0^g}/R_s$, affirming the scaling result obtained for the inertial limit, (35) and (36). The velocity of particle front for cases 1-2 and 1-5 reaches the maximum peak at a later time, again when the particle front crosses the secondary shock. For both cases, $t_{P2} = 3.2R_s/\sqrt{p_0^g/\rho_0^g}$. Furthermore, it is observed that the time for the particle front to overtake the gas contact, t_{P3}, for the two cases also agree well in dimensionless form, i.e., $t_{P3}\sqrt{p_0^g/\rho_0^g}/R_s = 4.1$.

Figure 4 shows the contour of maximum particle front velocity $u_{pf,max}$ as a function of d^p and R_s. Wide ranges of

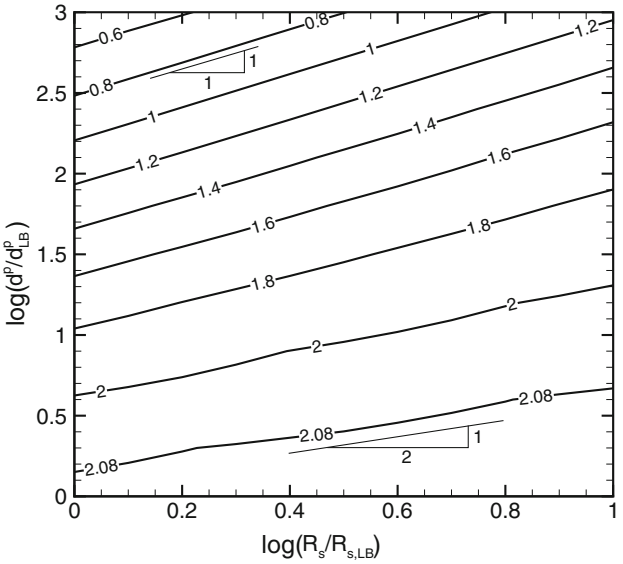

Fig. 4 Maximum particle front velocity as a function of R_s and d^p for $\rho^p = 1410\,\text{kg/m}^3$. The reference values for R_s and d^p are $R_{s,LB} = 25.4$ mm and $d^p_{LB} = 1\,\mu$m, respectively

d^p (1–1000 μm) and R_s (25.4–254 mm) are considered, and R_s and d^p are normalized by their lower bounds $R_{s,LB} = 25.4$ mm and $d^p_{LB} = 1\,\mu$m, respectively, where the subscript LB denotes the lower bound. The particle density is fixed at 1410 kg/m^3. Generally, u^p_{max} increases with decreasing d^p. For constant $u_{pf,max}$, d^p increases with R_s. For large d^p, particles are close to the inertial limit, and as a result the slopes of the contours are about 1. In contrast, small particles lie in the Stokes limit, and the slope is about 1/2. For intermediate d^p, the slope lies in between 1/2 and 1.

Relation between ρ^p and R_s Similar simulations are performed for varying ρ^p, while d^p is fixed, i.e., cases 1-1 and 1-6, and cases 1-3 and 1-5, to study the scaling relationship between ρ^p and R_s. For cases 1-1 and 1-6, $d^p = 1\,\mu$m. According to (34), St^p is the same as 0.0975 for the two cases, and thus, the particles lie in the Stokes limit. Based on the scaling analysis, the particle fronts shall collapse when plotted in terms of the dimensionless variables. This is confirmed by the simulation results of the position and velocity of the particle front as shown in Fig. 5a, b. For larger d^p, as the unsteady force becomes important, the scaling relation (33) becomes invalid. As a result, though ρ^p/R_s are the same for cases 1-3 and 1-5 ($d^p = 1$ mm), the position and velocity evolutions of the particle front are quite different even when they are plotted in terms of dimensionless variables.

Similar observations can also be made in Fig. 6, which shows contours of $u_{pf,max}$ with regard to R_s and ρ^p. In Fig. 6a, $d^p = 0.1$ mm and it can be observed that the contour lines are generally straight lines with a slope equal to 1. The linear

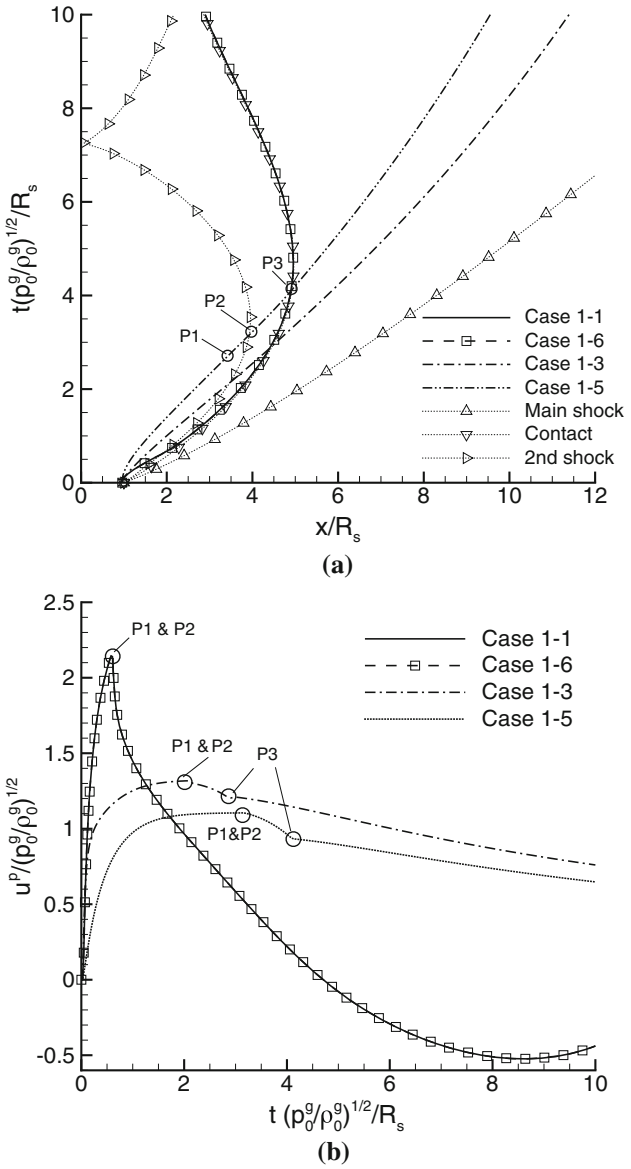

Fig. 5 Evolutions of particle position and velocity for different R_s and ρ^p. $d^p = 1\,\mu$m for cases 1-1 and 1-6, and $d^p = 1$ mm for 1-3, and 1-5. Note that ρ^p/R_s is identical for cases 1-1 and 1-6 and for cases 1-3 and 1-5. **a** x–t diagram. **b** u^p evolution

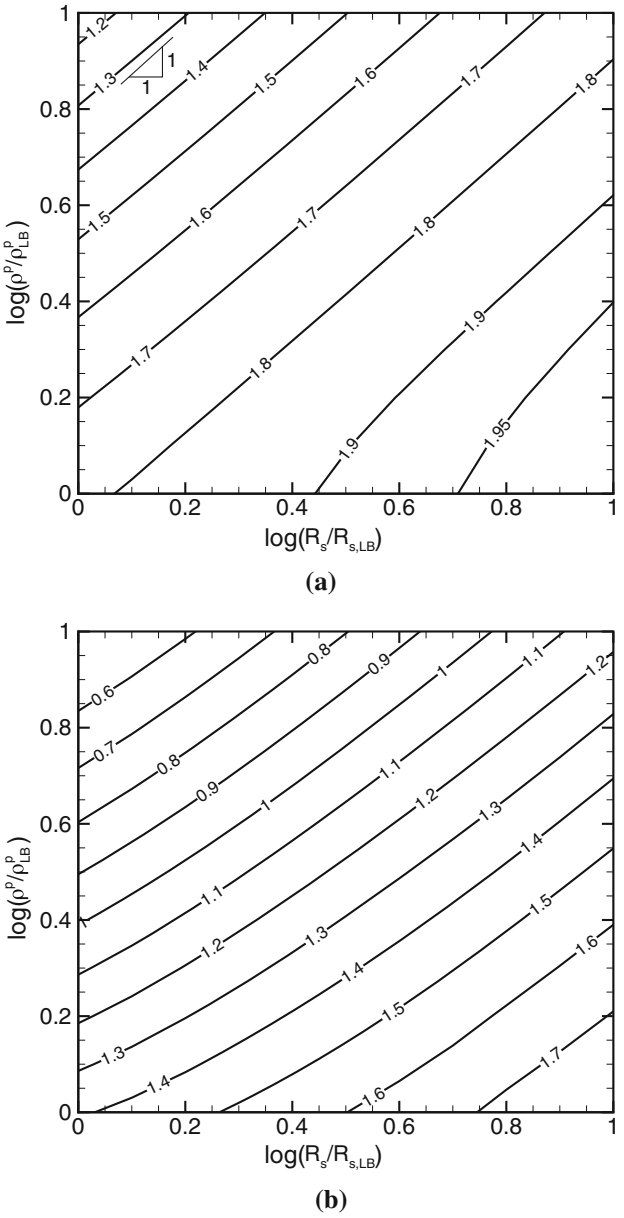

Fig. 6 Maximum particle front velocity as a function of R_s and ρ^p for $d^p = 0.1$ and 1 mm. The reference values for R_s and d^p are $R_{s,ref} = 25.4$ mm and $\rho^p_{ref} = 141\,\text{kg/m}^3$, respectively. **a** $d^p = 0.1$ mm. **b** $d^p = 1$ mm

relation between R_s and ρ^p breaks down when ρ^p is small, $\rho^p/\rho^p_{LB} < 0.2$, namely when the relative importance of the unsteady force increases. In Fig. 6b, $d^p = 1$ mm. For this large d^p, the unsteady force is important in general; therefore, the linear scaling relation between R_s and ρ^p is invalid in general. As a consequence, the contour lines in Fig. 6b are not straight and the slopes of which change with ρ^p and R_s.

3.5 An approximate scaling that incorporates initial pressure ratio

3.5.1 Approximate scaling for the gas flows

When $R_s \to 0$, the present problem of a finite-size-source blast reduces to a point-source blast considered by Sedov [52] and Taylor [53]. In the point-source blast, the initial conditions that characterize the gas solution are the total energy released E^g_{tot}. In [5], Brode employed E^g_{tot} to construct a length scale for the finite-size-source blast. His considera-

tion is mainly based on the argument that after a long enough time, the main shock wave engulfs a mass of air which is much larger than the initial mass of gas in the sphere, and then, the finite-size-source blast wave will merge to that generated by a point source. Therefore, instead of using R_s, he used $(E^g_{tot}/p^g_0)^{1/3}$ as the typical length scale. For the present problem, we consider the particle mass loading is small, and thus, the contribution of particles to the total energy is negligible. Then, the total energy of the sphere is dictated by the compressed gas as:

$$E^g_{tot} = \frac{4\pi (R_s)^3 p^g_4}{3(\gamma_4 - 1)}. \tag{37}$$

The corresponding length scale can be expressed as

$$\left(\frac{E^g_{tot}}{p^g_0}\right)^{1/3} = \left[\frac{4\pi}{3(\gamma_4 - 1)}\right]^{1/3} \left(\frac{p^g_4}{p^g_0}\right)^{1/3} R_s. \tag{38}$$

It is important to point out that (38) introduces a length scale that includes the initial gas pressure ratio p^g_4/p^g_0. (The corresponding time scale is $R_s(p^g_4/p^g_0)^{1/3}/\sqrt{p^g_0/\rho^g_0}$.) As will be shown below through the simulation results, $(p^g_4/p^g_0)^{1/3}$ is a very powerful scaling for the gas flow once we go pass the early evolution ($t \gg 0$).

3.5.2 Simulation results

Numerical simulations are performed to investigate the scaling of $(p^g_4/p^g_0)^{1/3}$. A summary of cases is given in Table 2.

The trajectories of the main shock wave, the contact discontinuity, and the secondary shock wave in the x–t diagram for cases 2-1 to 2-4 are shown in Fig. 7. For these two cases, p^g_4/p^g_0 are different, while $(p^g_4/p^g_0)/(\rho^g_4/\rho^g_0) = T^g_4/T^g_0 = 1$. It can be observed from Fig. 7a that the trajectories of the main shock, the contact discontinuity, and the secondary shock for the two cases collapse very well when $R_s(p^g_4/p^g_0)^{1/3}$ and $R_s(p^g_4/p^g_0)^{1/3}/\sqrt{p^g_0/\rho^g_0}$ are used to normalize space and time. It should be highlighted that p^g_4/p^g_0 for case 2-2 is ten times of that for case 2-1, yet the scaled results of the two cases agree remarkably well. Therefore, we can rewrite (27) in an approximate form as

Table 2 Case summary for Sect. 3.5.2. For all the cases $R_s = 25.4$ mm

Case	p^g_4/p^g_0	T^g_4/T^g_0
2-1	121	1
2-2	1210	1
2-3	121	10
2-4	1210	10

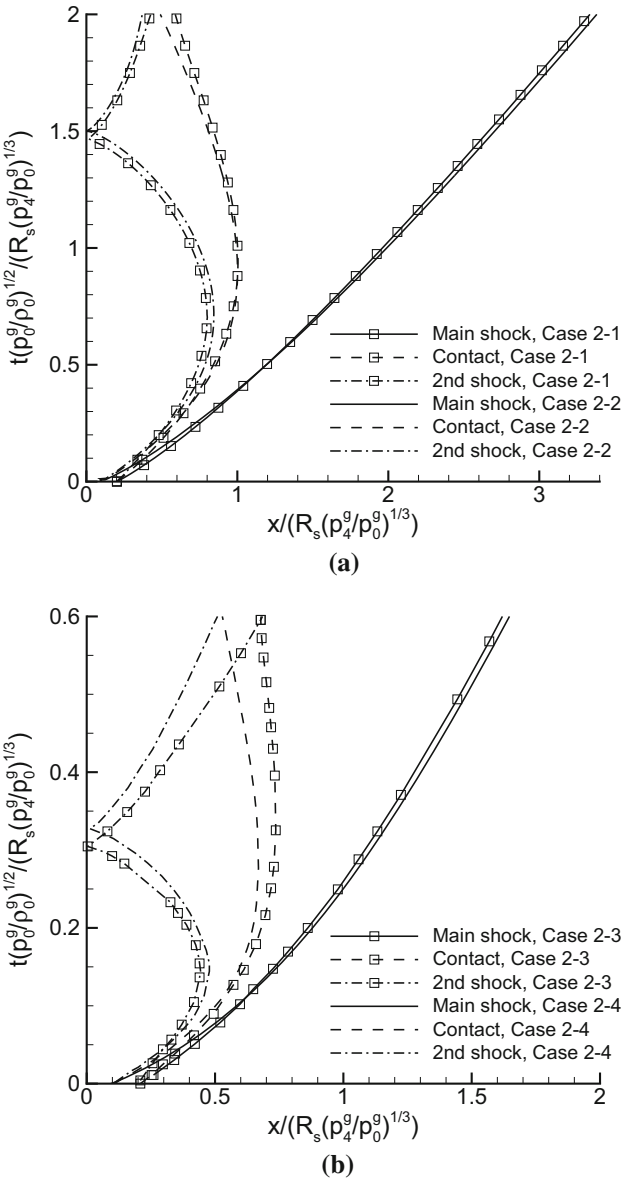

Fig. 7 Trajectories of the main shock wave, the contact discontinuity, and the secondary shock wave in x–t diagram for different p^g_4/p^g_0 and T^g_4/T^g_0. **a** $T^g_4/T^g_0 = 1$. **b** $T^g_4/T^g_0 = 10$

$$\frac{x_{gc}}{(p^g_4/p^g_0)^{1/3} R_s} \approx \xi\left(\frac{T^g_4}{T^g_0}, \gamma_4, \gamma_0, \frac{t\sqrt{p^g_0/\rho^g_0}}{(p^g_4/p^g_0)^{1/3} R_s}\right). \tag{39}$$

Here the expression is written for the gas contact, but which is applicable to the main shock and the secondary shock wave as well.

When we increase T^g_4/T^g_0 from 1 (cases 2-1 and 2-2) to 10 (cases 2-3 and 2-4), the gas flow changes substantially. The secondary shock reaches the origin much faster (as the sound speed in the compressed gas increases) and the reflected secondary shock overtakes the gas contact at an earlier time. As

a result, the gas contact does not bend much toward the origin compared to the cases with low T_4^g/T_0^g. Nevertheless, it can be observed from Fig. 7b that wave trajectories still collapse reasonably well when the new length and timescales are applied. This indicates that the scaling by $(p_4^g/p_0^g)^{1/3}$ and (39) remain reasonably appropriate even when T_4^g/T_0^g changes.

Figure 8 shows the variation of the characteristic time and spatial scales of gas flow (G1, G2, and G3) as functions of p_4^g/p_0^g and T_4^g/T_0^g. As described in Sect. 3.1, t_{G1} denotes the time for the secondary shock to reach the maximum distance, represented by x_{G1}; t_{G2} denotes the time for the gas contact to reach the maximum distance, x_{G2}; t_{G3} denotes the time for the secondary shock to reach the origin. It can be seen that when p_4^g/p_0^g varies from 121 to 1210, all the characteristic time and spatial scales obey the power law 1/3 quite well for $T_4^g/T_0^g = 1$ and 10. Further tests are also performed, showing that the scaling of $(p_4^g/p_0^g)^{1/3}$ is also valid for γ different from 1.4. If we further ignore the effect of γ_0 and γ_4, we obtain an asymptotic approximate similarity solution for the gas wave trajectories such as for the gas. For example, the time evolution of the gas contact location can be expressed as

$$\frac{x_{gc}}{(p_4^g/p_0^g)^{\alpha} R_s} \approx \xi \left(\frac{T_4^g}{T_0^g}, \frac{t\sqrt{p_0^g/\rho_0^g}}{(p_4^g/p_0^g)^{\beta} R_s} \right). \tag{40}$$

Here, the exponents α and β cannot be obtained by dimensional analysis, and data are generally required to obtain the values of α and β. In this study, we found that $\alpha = \beta = 1/3$ based on the total energy contained in the initial sphere, following the point-source theory for a spherical blast wave [5,53], which is then confirmed by simulation results.

3.5.3 Scaling and simulation results for the particle front

Due to the one-way coupling assumption, the particles here are dictated by the gas flows. Then, the asymptotic scaling of $(p_4^g/p_0^g)^{1/3}$ for the gas flow is ready to apply to the particle front. Figure 9 shows the time evolution of the particle front of two different particle sizes ($d^p = 1$ and 100 μm) for the gas flow cases 2-1 and 2-2. For the cases with $d^p = 1$ μm ($St^p \ll 1$), particles follow the surrounding gas closely. As a result, the scaling of $(p_4^g/p_0^g)^{1/3}$ works very well for the particles as well.

As the particle diameter increases, the particles fail to follow the gas flow due to their finite inertia. The trajectories of the particle front for the two different gas flows (cases 2-1 and 2-2) for $d^p = 100$ μm are quite different under the scaling of $(p_4^g/p_0^g)^{1/3}$, as shown in Fig. 9.

Figure 10 shows the characteristic locations where the particle front crosses the secondary shock (x_{P2}) and the contact surface (x_{P3}) (see Fig. 2), as function of p_4^g and d^p with ρ^p fixed as 141 kg/m^3. The pressure and particle diameter are normalized by reference values as $p_{ref} = 121 \times 10^5$ Pa and $d_{ref}^p = 1$ μm, respectively. The results for x_{P2} and x_{P3} are similar. For small particles, the contour lines are roughly straight lines, indicating the existence of the power-law relation between d^p and p_4^g. Consistent with the gas flow scaling, the slopes of the contour lines are about 1/3. As particle

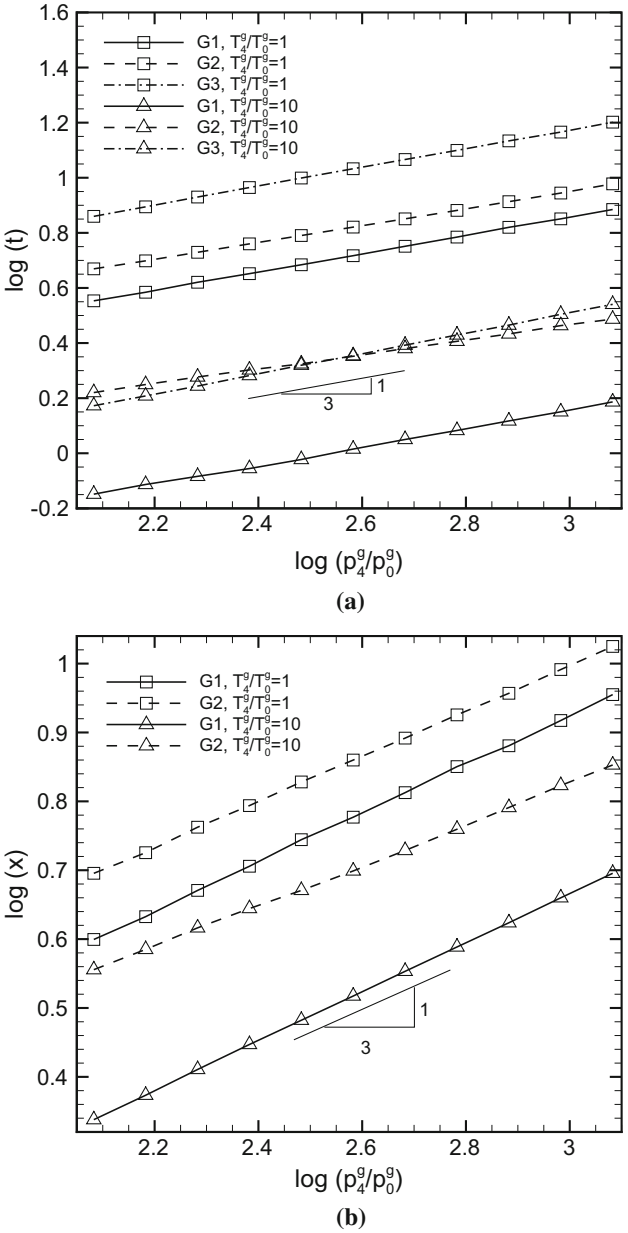

Fig. 8 Characteristic time and spatial scales of gas flow as functions of p_4^g/p_0^g for $T_4^g/T_0^g = 1$ and 10. Here, G1 denotes the time and location for the secondary shock to reach the maximum distance; G2 denotes the time and location for the gas contact to reach the maximum distance; G3 denotes the time for the secondary shock to reach the origin. **a** Timescales. **b** Spatial scales

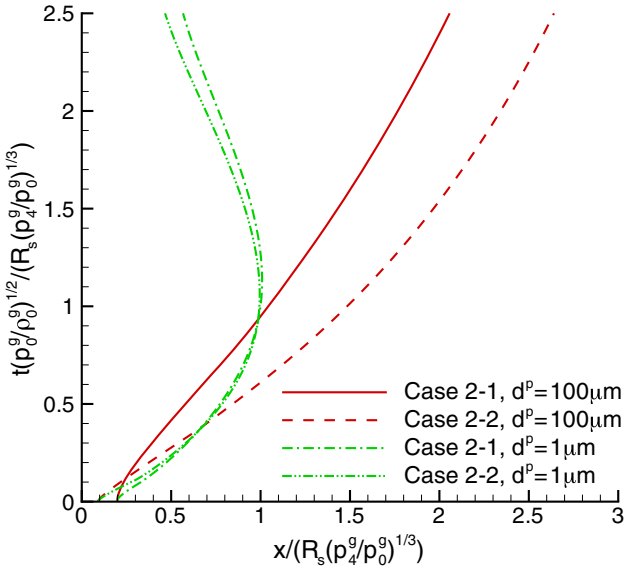

Fig. 9 Time evolution of particle front for cases 2-1 and 2-2 with $d^{\mathrm{p}} = 1$ and 100 μm

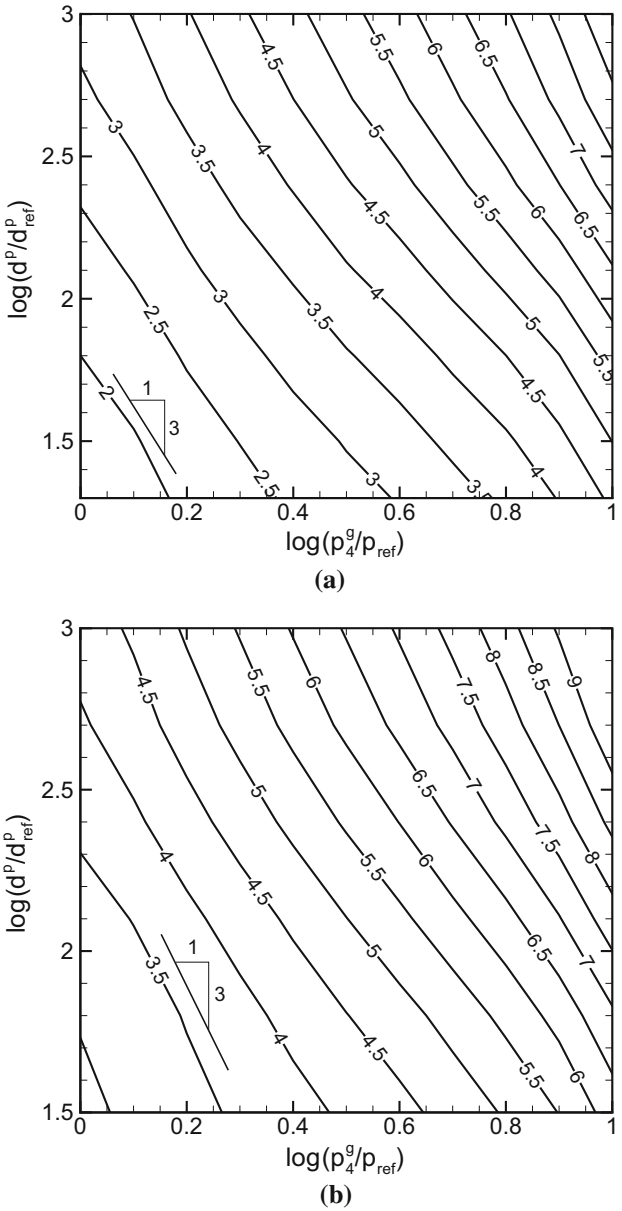

Fig. 10 Contour of characteristic locations, where the particle front crosses **a** the secondary shock (x_{P2}) and **b** the contact surface (x_{P3}) as functions of p_4^{g} and d^{p} with ρ^{p} fixed as 141 kg/m^3. The reference values for p_4^{g} and d^{p} are $p_{\mathrm{ref}} = 121 \times 10^5$ Pa and $d_{\mathrm{ref}}^{\mathrm{p}} = 1$ μm, respectively. **a** Crossing secondary shock. **b** Crossing contact

diameter increases, the contour lines are more complex, and a unique power-law scaling does not exist. Nevertheless, in general, 1/3 appears to be a quite good approximated scaling for a wide range of particle diameters.

4 Conclusions

Numerical simulation and scaling analysis are performed for a spherical particle-laden blast wave in the present study. The multiphase blast wave is generated by the sudden release of a sphere of compressed gas–particle mixture. Parametric studies are conducted to investigate the effects of the initial pressure and density ratios between the compressed gas and the ambient air, the density and diameter of particles on the time evolution of the main shock, the gas contact, the secondary shock, and the particle front. Scaling arguments are used to find the key dimensionless parameters. Under the one-way coupling assumption, the gas solution in dimensionless form can be fully determined by the initial pressure and density ratios, when R_{s} and $\sqrt{p_0^{\mathrm{g}}/\rho_0^{\mathrm{g}}}$ are used as the typical length and velocity scales. Due to the complexity of the drag force on the particles, additional dimensionless parameters arise, and as a result the particle front location does not linearly scale with R_{s} in general. Three asymptotic limits for the particles are then investigated, in which the particle front location becomes linearly scalable with R_{s}, as long as the corresponding dimensionless parameters remain constant. Following the point-source blast-wave theory, a length scale that incorporates the initial pressure ratio is proposed, i.e., $R_{\mathrm{s}}(p_4^{\mathrm{g}}/p_0^{\mathrm{g}})^{1/3}$. The simulation results show that the trajectories of the main shock, the gas contact, and the secondary shock for different pressure ratio collapse very well when the results are scaled by this length scale. This indicates that there exists an approximate similarity solution for the gas flows which is independent of the initial pressure ratio. For small particles, the particle front closely follows the gas contact, and thus, the scaling relation with regard to the initial pressure ratio is also effective in collapsing the particle front trajectories.

The present results are based on the one-way coupling approximation, but the scaling analysis can be extended to particle-laden blast waves with finite particle mass fractions. In particular, for small particles that can be considered to be in mechanical and thermal equilibrium with the surrounding gas, the two-way coupling effect can be incorporated by treating the gas–particle mixture as a "dusty gas" with modified density and specific heat ratio [54]. Therefore, it will be interesting to investigate the effect of the specific heat ratio on the scaling relations for the main shock and the contact discontinuity. Such an investigation is relegated to our future work.

Acknowledgements This work was supported by the US Department of Energy, National Nuclear Security Administration, Advanced Simulation and Computing Program, as a Cooperative Agreement under the Predictive Science Academic Alliance Program, under Contract No. DE-NA0002378. The authors would also acknowledge the support from the High Performance and Research Computing Services at Baylor University.

References

1. Chojnicki, K., Clarke, A.B., Phillips, J.C.: A shock-tube investigation of the dynamics of gas-particle mixtures: Implications for explosive volcanic eruptions. Geophys. Res. Lett. **33**, L15309 (2006). doi:10.1029/2006GL026414
2. Abbasi, T., Abbasi, S.A.: Dust explosions-cases, causes, consequences, and control. J. Hazard. Mater. **140**, 7–44 (2007). doi:10.1016/j.jhazmat.2006.11.007
3. Balakrishnan, K., Nance, D.V., Menon, S.: Simulation of impulse effects from explosive charges containing metal particles. Shock Waves **20**, 217–239 (2010). doi:10.1007/s00193-010-0249-z
4. Zhang, F., Frost, D.L., Thibault, P.A., Murray, S.B.: Explosive dispersal of solid particles. Shock Waves **10**, 431–443 (2001). doi:10.1007/PL00004050
5. Brode, H.L.: Numerical solutions of spherical blast waves. J. Appl. Phys. **26**, 766–775 (1955). doi:10.1063/1.1722085
6. Brode, H.L.: Theoretical solutions of spherical shock tube blasts. Technical Report RM-1974, Rand Corporation Report (1957)
7. Zarei, Z., Frost, D.L.: Simplified modeling of blast waves from metalized heterogeneous explosives simplified modeling of blast waves from metalized heterogeneous explosives. Shock Waves **21**, 425–438 (2011). doi:10.1007/s00193-011-0316-0
8. Boyer, D.W.: An experimental study of the explosion generated by a pressurized sphere. J. Fluid Mech. **9**, 401–429 (1960). doi:10.1017/S0022112060001195
9. Brode, H.L.: Blast wave from a spherical charge. Phys. Fluids **2**, 217–229 (1959). doi:10.1063/1.1705911
10. Liu, T., Khoo, B., Yeo, K.: The numerical simulations of explosion and implosion in air: use of a modified Harten's TVD scheme. Int. J. Numer. Methods Fluids **31**, 661–680 (1999). doi:10.1002/(SICI)1097-0363(19991030)31:4<661::AID-FLD866>3.0.CO;2-G
11. Friedman, M.P.: A simplified analysis of spherical and cylindrical blast waves. J. Fluid Mech. **11**, 1–15 (1961). doi:10.1017/S0022112061000810
12. McFadden, J.: Initial behavior of a spherical blast. J. Appl. Phys. **23**, 1269–1275 (1952). doi:10.1063/1.1702047
13. Ling, Y., Haselbacher, A., Balachandar, S.: Importance of unsteady contributions to force and heating for particles in compressible flows. Part 2: Application to particle dispersal by blast wave. Int. J. Multiph. Flow **37**, 1013–1025 (2011). doi:10.1016/j.ijmultiphaseflow.2011.07.002
14. Ling, Y., Haselbacher, A., Balachandar, S., Najjar, F.M., Stewart, D.S.: Shock interaction with a deformable particle: Direct numerical simulations and point-particle modeling. J. Appl. Phys. **113**, 013504 (2013). doi:10.1063/1.4772744
15. Milne, A.: Detonation in heterogeneous mixtures of liquids and particles. Shock Waves **10**, 351–362 (2000). doi:10.1007/s001930000062
16. Ripley, R.C., Zhang, F., Lien, F.S.: Shock interaction of metal particles in condensed explosive detonation. AIP Conf. Proc. **845**, 499–502 (2006). doi:10.1063/1.2263369
17. Zhang, F., Thibault, P.A., Link, R.: Shock interaction with solid particles in condensed matter and related momentum transfer. Proc. R. Soc. Lond. A Math. **459**, 705–726 (2003). doi:10.1098/rspa.2002.1045
18. Tanguay, V., Higgins, A., Zhang, F.: A simple analytical model for reactive particle ignition in explosives. Propellants Explos. Pyrotech. **32**, 371–384 (2007). doi:10.1002/prep.200700041
19. Balachandar, S., Eaton, J.K.: Turbulent dispersed multiphase flow. Annu. Rev. Fluid Mech. **42**, 111–133 (2010). doi:10.1146/annurev.fluid.010908.165243
20. Parmar, M., Haselbacher, A., Balachandar, S.: Generalized Basset-Boussinesq-Oseen equation for unsteady forces on a sphere in a compressible flow. Phys. Rev. Lett. **106**, 084501 (2011). doi:10.1103/PhysRevLett.106.084501
21. Parmar, M., Haselbacher, A., Balachandar, S.: Equation of motion for a sphere in equation of motion for a sphere in non-uniform compressible flows. J. Fluid Mech. **699**, 352–375 (2012). doi:10.1017/jfm.2012.109
22. Annamalai, S., Balachandar, S.: Faxén form of time-domain force on a sphere in unsteady spatially varying viscous compressible flows. J. Fluid Mech. **816**, 381–411 (2017). doi:10.1017/jfm.2017.77
23. Parmar, M., Haselbacher, A., Balachandar, S.: On the unsteady inviscid force on cylinders and spheres in subcritical compressible flow. Phil. Trans. R. Soc. A **366**, 2161–2175 (2008). doi:10.1098/rsta.2008.0027
24. Parmar, M., Haselbacher, A., Balachandar, S.: Improved drag correlation for spheres and application to shock-tube experiments. AIAA J. **48**, 1273–1276 (2010). doi:10.2514/1.J050161
25. Ling, Y., Haselbacher, A., Balachandar, S.: Importance of unsteady contributions to force and heating for particles in compressible flows. Part 1: Modeling and analysis for shock-particle interaction. Int. J. Multiph. Flow **37**, 1026–1044 (2011). doi:10.1016/j.ijmultiphaseflow.2011.07.001
26. Ling, Y., Wagner, J.L., Beresh, S.J., Kearney, S.P., Balachandar, S.: Interaction of a planar shock wave with a dense particle curtain: Modeling and experiments. Phys. Fluids **24**, 113301 (2012). doi:10.1063/1.4768815
27. Parmar, M., Haselbacher, A., Balachandar, S.: Modeling of the unsteady force for shock-particle interaction. Shock Waves **19**, 317–329 (2009). doi:10.1007/s00193-009-0206-x
28. Clift, R., Gauvin, W.H.: The motion of particles in turbulent gas streams. Proc. Chemeca **1**, 14–28 (1970)
29. Whitaker, S.: Forced convection heat transfer correlations for flow in pipes, past flat plates, single spheres, and for flow in packed beds and tube bundles. AIChE J. **18**, 361–371 (1972). doi:10.1002/aic.690180219
30. Ling, Y., Balachandar, S., Parmar, M.: Inter-phase heat transfer and energy coupling in turbulent dispersed multiphase flows. Phys. Fluids **28**, 033304 (2016). doi:10.1063/1.4942184
31. Ling, Y., Parmar, M., Balachandar, S.: A scaling analysis of added-mass and history forces and their coupling in dispersed multiphase

flows. Int. J. Multiph. Flow **57**, 102–114 (2013). doi:10.1016/j.ijmultiphaseflow.2013.07.005
32. Zarei, Z., Frost, D.L., Timofeev, E.V.: Numerical modelling of the entrainment of particles in inviscid supersonic flow. Shock Waves **21**, 341–355 (2011). doi:10.1007/s00193-011-0311-5
33. Balachandar, S.: A scaling analysis for point particle approaches to turbulent multiphase flows. Int. J. Multiph. Flow **35**, 801–810 (2009). doi:10.1016/j.ijmultiphaseflow.2009.02.013
34. Davis, S.L., Dittmann, T.B., Jacobs, G.B., Don, W.S.: Dispersion of a cloud of particles by a moving shock: Effects of the shape, angle of rotation, and aspect ratio. J. Appl. Mech. Tech. Phys. **54**(6), 900–912 (2013). doi:10.1134/S0021894413060059
35. Luo, K., Luo, Y., Jin, T., Fan, J.: Studies on shock interactions with moving cylinders using immersed boundary method. Phys. Rev. Fluids **2**, 064302 (2017). doi:10.1103/PhysRevFluids.2.064302
36. Mehta, Y., Neal, C., Jackson, T.L., Balachandar, S., Thakur, S.: Shock interaction with three-dimensional face centered cubic array of particles. Phys. Rev. Fluids **1**, 054202 (2016). doi:10.1103/PhysRevFluids.1.054202
37. Sridharan, P., Jackson, T.L., Zhang, J., Balachandar, S.: Shock interaction with one-dimensional array of particles in air. J. Appl. Phys. **117**, 075902 (2015). doi:10.1063/1.4913217
38. Mei, R., Adrian, R.J.: Flow past a sphere with an oscillation in the free-stream velocity and unsteady drag at finite Reynolds number. J. Fluid Mech. **237**, 323–341 (1992). doi:10.1017/S0022112092003434
39. Fox, T.W., Rackett, C.W., Nicholls, J.A.: Shock wave ignition of magnesium powders. In: Proceedings of 11th International Symposium Shock Tubes and Waves, pp. 262–268. University of Washington Press, Seattle, WA (1978)
40. Feng, Z.G., Michaelides, E.E.: Unsteady heat transfer from a sphere at small peclet numbers. J. Fluid Eng. Trans. ASME **118**, 96–102 (1996). doi:10.1115/1.2817522
41. Roe, P.L.: Approximate Riemann solver, parameter vectors, and difference schemes. J. Comput. Phys. **43**, 357–372 (1981). doi:10.1006/jcph.1997.5705
42. Jiang, G.S., Shu, C.W.: Efficient implementation of weighted ENO schemes. J. Comput. Phys. **126**, 202–228 (1996). doi:10.1006/jcph.1996.0130
43. Barth, T.J.: A 3D upwind Euler solver for unstructured meshes. AIAA Paper 91-1548 (1991). doi:10.2514/6.1991-1548
44. Haselbacher, A.: A WENO reconstruction algorithm for unstructured grids based on explicit stencil construction. AIAA Paper 2005-0879 (2005). doi:10.2514/6.2005-879
45. Haselbacher, A., Najjar, F., Ferry, J.: An efficient and robust particle-localization algorithm for unstructured grids. J. Comput. Phys. **225**, 2198–2213 (2007). doi:10.1016/j.jcp.2007.03.018
46. Ling, Y., Haselbacher, A., Balachandar, S.: A numerical source of small-scale number-density fluctuations in Eulerian-Lagrangian simulations of multiphase flows. J. Comput. Phys. **229**, 1828–1851 (2010). doi:10.1016/j.jcp.2009.11.011
47. Mankbadi, M.R., Balachandar, S.: Compressible inviscid instability of rapidly expanding spherical material interfaces. Phys. Fluids **24**(3), 034106 (2012). doi:10.1063/1.3689183
48. Takayama, K., Kleine, H., Grönig, H.: An experimental investigation of the stability of converging cylindrical shock waves in air. Exp. Fluids **5**, 315–322 (1987). doi:10.1007/BF00277710
49. Frost, D.L., Goroshin, S., Ripley, R., Zhang, F.: Jet formation during explosive particle dispersal. Military Aspects of Blast and Shock 21, Jerusalem (2010)
50. Xu, T., Lien, F.S., Ji, H., Zhang, F.: Formation of particle jetting in a cylindrical shock tube. Shock Waves **23**, 619–634 (2013). doi:10.1007/s00193-013-0472-5
51. Clift, R., Grace, J.R., Weber, M.E.: Bubbles, Drops, and Particles. Dover, New York (1978)
52. Sedov, L.I.: Similarity and Dimensional Methods in Mechanics. Academic Press, New York (1959). doi:10.1016/B978-1-4832-0088-0.50001-3
53. Taylor, G.I.: The formation of a blast wave by a very intense explosion. I. Theoretical discussion. Proc. R. Soc. Lond. A Math. **201**, 159–174 (1950). doi:10.1098/rspa.1950.0049
54. Marble, F.E.: Dynamics of a dusty gas. Annu. Rev. Fluid Mech. **2**, 397–446 (1970). doi:10.1146/annurev.fl.02.010170.002145